Internal tides and baroclinicity in the southern Weddell Sea 1. Model description

Robin Robertson

Lamont-Doherty Earth Observatory, Columbia University, Palisades, New York, USA

Abstract. Near the continental shelf break in the southern Weddell Sea, Warm Deep Water and Western Shelf Water meet. Mixing mechanisms, such as internal tides, have the potential to mix these water masses and form Antarctic Bottom Water. A modified version of the Princeton Ocean Model was utilized to investigate the internal tidal fields generated by the interaction of the M_2 barotropic tide with topography for transects across the continental shelf and slope in the southern Weddell Sea. Internal tides were generated over the upper continental slope as predicted by linear internal wave theory. Although the essentially two-dimensional domain resulted in differences between the model elevations and the observations exceeding the observational uncertainties, the cross-slope velocities agreed well with differences less than the uncertainties for 78% of the existing observations.

1. Introduction

The Weddell Sea is the major single source of Antarctic Bottom Water (AABW), providing most of the deep and bottom water for the Southern Ocean [*Weppernig et al.*, 1996]. Weddell Sea Deep Water (WSDW), a subclass of AABW [*Carmack*, 1977], is formed through several different combinations of water masses [*Gordon*, 1998]. The two most commonly occurring combinations mix Warm Deep Water (WDW) with either Western Shelf Water (WSW) or Ice Shelf Water (ISW) [*Gordon*, 1998]. Modified versions of these two mixing schemes also incorporate Winter Water (WW) and/or Modified Warm Deep Water (MWDW) [*Foldvik et al.*, 1985; *Foster and Carmack*, 1976; *Gordon*, 1998]. The potential for AABW formation increases at locations where these water masses lie in close proximity, for example, the upper continental slope in the southern Weddell Sea (Figure 1a). Figure 1a shows typical locations of these water masses in a transect across the continental slope in the southern Weddell Sea taken from observations. Because of the potential for AABW formation, processes that cause mixing of WDW with either WSW or ISW are of significant interest to large-scale modeling efforts.

Tides are recognized as a significant factor in ocean mixing [see *Munk and Wunsch*, 1998]. They have been observed to increase mixing in regions as diverse as the Indonesian seas [*Ffield and Gordon*, 1996; *Hatayama et al*., 1996], the deep ocean [*Polzin et al.*, 1997], and the Arctic Ocean [*Padman et al*., 1992; *Polyakov*, 1995]. Ocean mixing is affected by tides through several mechanisms. Interactions between the barotropic tide and topography, such as ridges or the continental slope, generate baroclinic tides, internal waves, and continental shelf waves. *Munk and Wunsch* [1998] postulate that ~200-600 GW (1 GW = 10^9 W) or 22-67% of the 900 GW of worldwide barotropic tidal energy loss occurs over deep sea ridges. A larger amount of energy is likewise lost over continental boundaries. Baroclinic tides set up the conditions for shear or advective instabilities, which can increase mixing between the WDW and the surface waters and contribute to the heat transfer through the upper ocean [*Robertson*, 1999].

Do internal tides occur in the Weddell Sea? If so, are they energetic enough to significantly influence other oceanic processes such as AABW formation, upper ocean heat fluxes to the sea ice, or upper ocean tidal currents? A few observations indicate the presence of internal tides. Their locations are shown by stars in Figure 2a. Analyses of mooring data from the southern shelf and slope by *Middleton and Foster* [1977] showed that semidiurnal tidal currents in a benthic layer extending to 100 m above the seabed were strongly depth-dependent. They described these tides as "baroclinic"; however, in a later paper [*Foldvik et al.*, 1990] they noted that the vertical structure was consistent with the ocean's barotropic response when tidal constituents were close to their critical latitude, i.e., the latitude at which the tidal frequency equals the Coriolis frequency f. There are two issues here that are relevant to later discussions. First, throughout most of the Weddell Sea, f is close to the frequency of the dominant semidiurnal M_2 tidal constituent, and thus short data records cannot distinguish between near-inertial motion and tidal motion. Thus the tidal observations, particularly those with short records, may include inertial oscillations in their estimates for the tidal signal. Second, vertical structure of tidal currents can exist under certain circumstances because of frictional considerations, even without any density stratification

[*Sverdrup*, 1927; *Lamb*, 1945; *Furevik and Foldvik*, 1996]. Regardless of whether friction or internal tides or some combination of both are responsible for the vertical structure of the velocity fields, vertical shear in the water column can lead to mixing. Therefore, for this investigation, tidal mixing will include both mixing due to internal tides and due to increased benthic boundary effects resulting from the tidal velocities.

Other observations of semidiurnal-band ocean variability in the Weddell Sea have been reported by *Foldvik et al*. [1990], *Foster* [1994], *Robertson et al.* [1995], and *Levine et al*. [1997]. *Foster* [1994] saw large vertical displacements of the pycnocline in 1 day of conductivity-temperature-depth (CTD) data in the northwestern Weddell Sea, while *Robertson et al*. [1995] found strong semidiurnal-band velocity shear across the pycnocline in the eastern Weddell Sea near Maud Rise. *Levine et al.* [1997] found an increase in internal wave energy levels in shallower water further up the continental slope, which they attributed to internal wave activity. Recently recovered current meter moorings from the northern Filchner Trough [*Woodgate et al*., 1998] show similar semidiurnal-band velocity structure to that described as due to frictional effects by *Foldvik et al*. [1990]; however, their sites are in a location where no M_2 internal wave generation is expected according to linear internal wave theory (see section 3.1).

The available database (stars in Figure 2a and stars and triangles in Figure 2b) is clearly inadequate for evaluating the overall relevance of baroclinic tides to Weddell Sea oceanography. *Robertson et al*. [1998] (hereinafter referred to as RPE) developed a high-resolution, depth-integrated ocean tidal model to improve our understanding of the distribution of barotropic tidal kinetic energy in the Weddell Sea. Using these tidal velocity fields, a parameterization of the energy flux going from the barotropic to the baroclinic tide suggested that baroclinic tides may be strong enough to play a role in water mass modification near the shelf break (Figure 3a).

Motivated by these previous studies, the primary goal of this study was to improve the understanding of internal tide generation and propagation beyond the simple parameterization of baroclinic tides described by RPE. The area of focus is the southern shelf and slope of the Weddell Sea since this is the region in which tidal kinetic energy is known to be strong and simple models suggest that the baroclinic tide should be significant (Figure 3a). For this investigation a numerical model (a modified version of the Princeton Ocean Model) was used in an attempt to simulate internal tide generation for conditions that are typical of the southern Weddell Sea shelf and slope.

The numerical model is described in section 2. The Princeton Ocean Model (POM) and other models have been successfully used to determine the internal tidal fields in midlatitude regions such as the Hudson-Raritan Basin [*Oey*, 1985a; 1985b], the Hebrides Sea [*Xing and Davies*, 1996], Monterey Bay [*Petruncio*, 1996], the Australian Northwest Shelf [*Holloway*, 1996], and Georges Bank [*Chen and Beardsley*, 1998]. Theoretical considerations for different wave types, including internal waves, and their generation and propagation are discussed in section 3. Section 4 evaluates the model results, including comparisons with existing observations. A summary is provided in section 5. In the companion paper [*Robertson*, this issue] the sensitivity of the tidal dynamics to the effects of the critical latitude and stratification are investigated.

2. Modeling Approach

2.1. Model Description

A modified version of POM was utilized to simulate the generation and propagation of internal tides for two-dimensional cross sections over the continental shelf and slope. POM has been previously applied for this purpose in midlatitude regions by *Holloway* [1996] and *Chen and Beardsley* [1998]. Only the major points and the modifications of POM will be covered here; a full description of POM is given by *Mellor* [1993]. The two major modifications to POM were an adjustment of the density determination and the inclusion of an ice shelf (for a full description, see *Robertson et al*. [2001]).

POM is a three-dimensional, nonlinear, primitive equation model developed by *Blumberg and Mellor* [1987]. The model has a free surface and makes both the Bousinessq and hydrostatic approximations. It uses the Mellor-Yamada level 2.5 turbulence closure scheme for vertical mixing of momentum, heat, and salt. The Smagorinsky diffusivity scheme was used to determine the horizontal momentum viscosity and horizontal temperature and salinity diffusivity coefficients. In this scheme, diffusivity is dependent on grid size and horizontal velocity shear as well as an adjustable constant. This constant was set to 0.2 as suggested by the model developers, although smaller values have been used [*Oey*, 1985a]. Typical values for the horizontal viscosity ranged from 0 to 12 $m^2 s^{-1}$. Normalized density ρ' (dimensionless) is determined from the potential temperature θ and salinity S fields using the United Nations Educational, Scientific, and Cultural Organization (UNESCO) equation of state and normalized by a mean density ρ_o (kg m^{-3}) [*Mellor*, 1993]. In this modification of POM, density was not adjusted for pressure in order to avoid an error, which results near the critical latitude [*Robertson et al.*, 2001]. POM was also modified to accommodate the existence of an ice shelf as a frictional stress surface by adding a

surface stress term. This surface stress term reflects the friction against the ice shelf and is handled in a similar manner as the bottom frictional stress. The ice shelf was assumed to float. Melting of the ice shelf was not included since even high melt values of ~7 m yr^{-1} [*Makinson and Nicholls*, 1999] result in a melt of < 1 m over the duration of a run. This change is negligible with the topography of the model, especially when considering its accuracy [*Padman et al*., 1999]. Density changes due to melting were ignored. The hydrography in this application did not include ISW and was not realistic under the ice shelf. Consequently, the flow under the ice shelf was not expected to be realistic and was not evaluated in the results section. Sea ice was not included in the model. A quadratic stress formulation was used for both the sea bed and the ice shelf with the drag coefficient C_D = 0.0025. Because of the existence of an ice shelf over part of the domain, boundary layers were used at both the surface and bottom. The leapfrog scheme is used for time stepping. The model utilizes the "barotropic-baroclinic mode" splitting technique to reduce the time step required for stability. A "barotropic" time step of 2 s was used, which was within the stability requirement of the Courant-Friedrichs-Lewy condition for the grid size and domain bathymetry [*Haltiner and Williams*, 1980, p. 119]. A "baroclinic" time step of 72 s was used. The simulations were run for 46 days, which was sufficient for the domain-integrated energy in the baroclinic mode of the model to stabilize, ~40 days.

2.2. Model Domain, Grid, Bathymetry, and Initial Hydrography

Two transects across the continental shelf-slope break were selected as the model domains. The transect locations are shown as dashed lines in Figure 2b and represent different slope steepnesses, transect B being steeper than transect A. They were also selected to be aligned with the direction of tidal propagation at the continental shelf-slope break and to pass in the vicinity of existing tidal observations (triangles and stars in Figure 2b). Because of the curving coastline of this region, however, the direction of tidal propagation varies over the transects and only is aligned with the transects at the continental shelf-slope break. The transects are also roughly perpendicular to the continental shelf-slope break.

The model uses an Arakawa C grid in the horizontal dimensions. Although the model was operated in a three-dimensional mode, this was essentially a two-dimensional application, using the cross-slope y and vertical z directions. The grid was composed of five cells in the along-slope direction x and 600 in the cross-slope direction y. The horizontal grid spacing was 2 km in both the along-slope and cross-slope directions. The model utilizes a sigma coordinate system with σ scaled to the sum of the water column thickness $H(y)$ and the surface elevation $\eta(y,t)$. This quantity is also defined as the effective water depth $D(y,t)$ ($D(y,t) = H(y) + \eta(y,t)$). Under the ice shelf the coordinate system is offset from the surface by the ice shelf thickness in order to account for the pressure head associated with the ice shelf. Sixty-six sigma levels were used, of which 60 were spaced evenly through the water column between the numerical boundary layers, which consisted of three sigma layers each. These three sigma layers occupy the equivalent of one of the midwater column sigma layers, and their thicknesses decreased as 0.5, 0.25, and 0.25 of one of the midwater column layer heights, respectively, with the smaller sigma layers near the surface and the bottom.

Modified ETOPO5 bathymetry was used for the model depth [*Natonal Geophysical Data Center*, 1992], with the modifications described by RPE. Estimates of the bathymetry under the Filchner-Ronne Ice Shelf and ice shelf thickness came from the map of *Vaughan et al.* [1994]. The topography was modified to have open boundaries at both ends by limiting the ice shelf depth to 340 m for transect A and the bottom to 550 m for transect B. Since the real three-dimensional flow is not blocked by Berkner Island but flows under the ice shelves at the southern end, an open boundary is required in the two-dimensional application to simulate equivalent topographic conditions, i.e., an open basin. With a wall at the southern boundary this two-dimensional application would be that of a closed basin, and a standing wave would be set up by the wave reflecting from the southern end.

Austral winter conditions were used for the initial potential temperature θ and salinity S fields. As seen in the observed summer θ field near the transect (Figure 1a), a shelf break front exists. In order to simulate the shelf break front, different hydrographic profiles were used over the deep basin and the continental shelf, with a transition zone occurring over the upper continental slope. The deep water hydrography was primarily taken from the observations of Ice Station Weddell [*Huber et al*., 1994] and verified against the observations of *Foster and Carmack* [1976]. Over the shelf, profiles were estimated from the observations of *Gammelsrød et al.* [1994], *Foster et al*. [1987], and *Foster and Carmack* [1976]. The observed fields were smoothed below the permanent pycnocline to remove apparent instabilities. The resulting deep water profiles of θ, S, potential density σ_θ, and the Brunt-Väisälä frequency N are shown as solid lines in Figures 4a-4d, respectively, and the corresponding shelf profiles are shown as shaded lines. The Brunt-Väisälä frequency N (s^{-1}) was determined from the stratification according to

$$N = \left(\frac{-g}{\rho_o} \partial \rho_s / \partial z \right)^{1/2}, \quad (1)$$

where ρ_s is the nonnormalized in situ density (kg m^{-3}). The mean density ρ_o was 1027.8 kg m^{-3}, and the gravitational acceleration g was 9.8 m s^{-2}. Despite the smoothing of the θ and S fields, some irregularities are present in N below 3000 m (Figure 4d).

The resulting initial θ and S fields are shown in Figures 1b and 1c, respectively. The model hydrography was both simplified and smoothed compared to the observed hydrography (θ shown in Figure 1a) but reproduced the major features. Unfortunately, much of the observational data did not extend to the bottom, and the water depth in Figure 1a represents the extent of the observations. The upper 100 m of the observations disagree with the model fields since the model represents winter conditions and most of the observations were collected in summer. Smoothing and the use of only two profiles to characterize the deep and shallow water columns resulted in other differences between the model and observational fields, which included a surface layer, no downwelling of the water masses from ~1000 to 1100 m along the transect, slightly shallower WSDW than in the observations, and absence of WSBW in the observations because of their shallower depth. Despite these differences the idealized model hydrography faithfully represented the major features such as the water masses and the shelf break front. The same hydrography was used for both transects.

2.3. Boundary Conditions and Forcing

Since land was not included in the model domain, four open boundaries were present. The cross-slope running open boundaries, had periodic boundary conditions for all variables, i.e., the variables are identical on these boundaries. In this application this condition along with the geometry of the domain resulted in all variables being constant in the along-slope direction ($\partial / \partial x = 0$). At both the deep basin and continental shelf open boundaries, tidal forcing was implemented by setting the elevations η using coefficients taken from a barotropic model of the Weddell Sea (RPE). Only the most energetic constituent, M_2, was used for tidal forcing. The tidal forcing was modified by a ramp over the first day to reduce the high-frequency noise generated by an initial impulse [*Holloway*, 1996].

After consideration of several alternative open boundary conditions [*Palma and Matano*, 1998], the *Lewis et al.* [1994] partially clamped radiative boundary condition was chosen for the depth-independent cross-slope velocity V_A and an advective scheme was chosen for depth-independent along-slope velocities U_A on the shelf (southern) and deep basin (northern) boundaries [*Petruncio*, 1996]. The boundary conditions for V_A were tuned as suggested by *Lewis et al.* [1994] in order to achieve elevation amplitudes comparable to the specified elevation. *Martinsen and Engedahl*'s [1987] flow relaxation scheme was used over five cells for the depth-dependent horizontal velocities, U and V, at both the shelf and deep basin boundaries. A detailed description of Martinsen and Engedahl's boundary scheme is given by *Holloway* [1996]. The boundary conditions for the vertical velocity W were no flow through the surface and bottom sigma layers and zero at the open continental shelf and deep basin boundaries. The open continental shelf and deep basin boundary conditions for θ and S also used *Martinsen and Engedahl*'s [1987] flow relaxation scheme.

3. Theoretical Considerations

3.1. Wave Types and Wave Generation

In the Southern Ocean the M_2 tide consists primarily of a barotropic Kelvin wave propagating westward around Antarctica. Even without stratification, interaction of the tide with topography may cause the excitation of inertial oscillations, gyroscopic waves, and/or barotropic Poincaré waves [*LeBlond and Mysak*, 1978; *Huthnance*, 1981; *Middleton and Denniss*, 1993; *LeTareau and Maze*, 1996]. Where stratification exists, variations in topography may convert some of the barotropic Kelvin wave energy to baroclinic Kelvin waves [*Baines*, 1986], baroclinic Poincaré waves, or higher-frequency internal gravity waves [*Gill*, 1982, p. 142]. Higher-frequency internal waves may also be generated through nonlinear interactions and result in energy being transferred to harmonics of the original frequency.

Generation of internal waves is primarily dependent on the steepness of the topography, the strength of the barotropic current, and the stratification. *Baines* [1986] developed a parameter for determining the necessary conditions for internal wave generation. This parameter γ is the ratio of the bottom slope, $\partial H / \partial y$, to the slope of the internal wave characteristic α, i.e.,

$$\gamma = \frac{\partial H / \partial y}{\alpha}, \tag{2}$$

where

$$\alpha = \left(\frac{\omega^2 - f^2}{N^2 - \omega^2} \right)^{1/2}. \tag{3}$$

Here ω is the wave frequency (s^{-1}) and f is the Coriolis parameter (s^{-1}), determined from $f = 2\ \Omega \sin \psi$, where Ω is the Earth's angular rotation ($7.292 \times 10^{-5}\ s^{-1}$) and ψ is the latitude. For internal tides, ω is the tidal frequency ($1.40518 \times 10^{-4}\ s^{-1}$ for M_2). The value of N near the seabed is used for this calculation.

When $\gamma \approx 1.0$, the slope is critical, and resonant phenomena cause the generation of internal waves to be the greatest. Internal waves generated on a critical slope propagate along the slope since their ray paths follow the slope. Where γ is < 1.0, the slope is called subcritical, and fewer internal waves are generated. Waves which are formed may propagate either onshore or offshore. Where γ is > 1.0, the slope is supercritical, and internal waves may be generated but only propagate offshore [*Sherwin*, 1991]. Note that as $\omega \rightarrow f$, $\alpha \rightarrow 0$; consequently, even for weakly stratified conditions (small N), gentle bottom slopes can lead to a critical or supercritical values for γ. Since internal wave generation occurs not only exactly at $\gamma = 1$ but also in a band around this value, a range between 0.5 and 2.0 was defined as the range of critical γ, with values below this range being subcritical and values above being supercritical.

The value of γ for the M_2 frequency was estimated for the southern Weddell Sea (Figure 3b). For this calculation a generalized N was used that was dependent on the water depth, with N equal to 2.0 cph for depths < 500 m, varying linearly from 2.0 to 0.2 cph for depths between 500 and 1000 m, and equal to 0.2 cph for depths below 1000 m. This estimate predicts that internal tides can be generated in localized areas along the continental shelf break with water depths of ~500 to 800 m and that a critical slope region exists within transect A and a supercritical region exists within transect B.

The value of $\gamma(M_2)$ was also determined for transect A using N at the bottom as determined from the model's initial hydrography. The value of $\gamma(M_2)$ (solid line in Figure 5a) is critical over the upper continental slope from roughly 525 to 600 km distance from the transect origin (See Figure 5c for the topography). The generally subcritical values of γ are due to the weak stratification.

The latitude where the tidal frequency ω equals the inertial frequency f is referred to as the critical latitude ψ_{crit}. The ψ_{crit} for M_2 is at $74^o28.5'S$, which is near the continental shelf break, 522 km from the origin of the transects (Figures 2b and 5b). Since at ψ_{crit}, $f = -\omega$ (Southern Hemisphere), α becomes zero, and γ goes to infinity. Obviously, the linear theory used to determine γ fails at this point, and $\gamma(M_2)$ is not shown poleward of ψ_{crit} in Figure 5a.

If the domain is shifted northward 10^o so that ψ_{crit} is no longer in the domain, γ never reaches the critical level (dashed line in Figure 5a). With the steeper topography of transect B (Figure 5f), $\gamma(M_2)$ is critical over a narrow region of the continental slope (Figure 5d).

3.2. Wave Propagation

While the regions for wave generation may be highly localized, the resultant waves may be observed over a broader area, dependent on their propagation characteristics. Wave propagation is characterized by the dispersion relation and the horizontal group speed c_g. These relations are shown in Table 1 for Kelvin waves, Poincaré waves, gyroscopic waves, and internal waves, where k, l, and m are the along-slope, cross-slope, and vertical wave numbers (m^{-1}), respectively. Most of the tidal energy in the Weddell Sea propagates as a barotropic Kelvin wave, independently of changes in latitude, with c_g dependent only on the water column thickness (Table 1). However, in some areas tidal energy propagates as Poincaré waves and is dependent on latitude ψ through f. Since $|\omega| > |f|$ for M_2 Poincaré waves, they do not develop poleward of ψ_{crit}. Furthermore, ψ_{crit} acts as a turning latitude, ψ_{turn}, for poleward propagating Poincaré waves and prevents them from propagating farther poleward. *Middleton and Denniss* [1993] note the turning latitude ψ_{turn} does not always coincide with ψ_{crit}; however, using their evaluation for the transect resulted in $\psi_{turn} \approx \psi_{crit}$ (~ 5 km south). It should be noted that owing to the long barotropic wavelengths (Table 1), ψ_{crit} does not act as a complete wall, but some energy to propagates through. This also holds for reflection from the slope since the wavelengths are long

in comparison to the shelf width (~150 km). The propagation of gyroscopic waves is latitude-dependent through *f*, and they do not develop equatorward of ψ_{crit}. Their internal wave dispersion relation and group speed are also dependent on latitude (Table 1).

To investigate the propagation rate of internal waves, the cross-slope component of the internal horizontal group speed c_g was determined using

$$c_g = \partial\omega / \partial l = \frac{N^2}{m\omega}\left(\frac{\omega^2 - f^2}{N^2 - f^2}\right)^{1/2} \tag{4}$$

[*Gill*, 1982, pp. 261]. This formulation is equivalent to that in Table 1 when the Wentzel-Kramer-Brillouin (WKB) approximation (*N(z)* varies slowly) is used and

$$m^2 = \frac{l^2\left(N^2 - \omega^2\right)}{\omega^2 - f^2} \ . \tag{5}$$

For the purpose of calculating typical values the internal waves were assumed to be of mode one (i.e., $m=\pi H^{-1}$), where *H* is the water column thickness. The estimated values of c_g for both transects A and B are low, roughly 1-6 cm s^{-1}, for the M_2 internal tides over the upper continental slope and decrease to zero at ψ_{crit}, as seen by the solid lines in Figures 5b and 5e, respectively. Owing to low c_g values resulting from weak stratification and the proximity to ψ_{crit}, propagation of internal tides away from the generation site is extremely slow. When the domain is moved north 10^o so that ψ_{crit} is no longer in the domain, c_g increased (dashed line in Figure 5b).

Another way to examine internal waves is through internal wave ray theory, which says locally generated internal tidal energy should propagate along internal wave ray paths. Characteristic ray paths for the M_2 internal tides for the latitude, stratification, and topography of the model domain are shown in Figure 6a. The weak stratification results in steep ray paths. Internal wave rays are absent poleward of the critical latitude. Over the upper slope where γ is critical, the angle of the internal wave rays is nearly parallel to the bottom slope. Figure 6b shows the corresponding ray paths for the stratification and domain if the latitude was shifted 10^o to the north, so ψ_{crit} was not in the domain. Internal wave rays exist throughout the domain but are not parallel to the bottom slope since γ (M_2) is subcritical. Any internal tides, which are generated, will propagate away from the generation site faster since values of c_g for this scenario are larger (dashed line in Figure 5b) than those at the original latitude.

The foregoing discussion has been based on linear theory, and there is a question of how well this theory approximates reality. *Eriksen* [1998] investigated internal wave reflection and mixing at Fieberling Guyot and found that the linear theory for generation and reflection of internal waves off a sloping bottom predicted the enhanced peak at the frequency of the critical slope quite well. However, he noted that the linear wave theory failed to predict either the amplitude of the peak or the off-slope decay scale. Linear wave theory neglects advection, frictional stress, and other nonlinear effects that POM includes. Consequently, differences are expected between POM results and linear theory predictions.

3.3. Boundary Layer Effects

Frictional stress induces boundary layers both at the seabed and at the surface under the ice shelf. Both the boundary layers and the vertical structure of the horizontal velocities can be affected by proximity to the critical latitude. To evaluate this effect, it is useful to decompose the tidal velocity into two rotary components, clockwise and counterclockwise. These components respond differently to proximity to ψ_{crit}. The amplitude of the positive rotary current (counterclockwise) should be depth-dependent, and the amplitude of the negative rotary current (clockwise) should be depth-independent in the Southern Hemisphere [*Prinsenberg and Bennett*, 1989; *Foldvik et al*., 1990]. *Furevik and Foldvik* [1996] used a formulation for the boundary layer thickness scale for the two rotary components (λ_+ and λ_-, respectively). The boundary layer thickness is defined as the distance that the velocity magnitude is reduced by e^{-1}, and the scales can be approximated by

$$\lambda_+ = \sqrt{\frac{K_M}{\omega + f}} \qquad \lambda_- = \sqrt{\frac{K_M}{\omega - f}} \ , \tag{6}$$

where K_M is a constant vertical eddy viscosity ($m^2\ s^{-1}$). Over the upper continental slope at the latitude for the model domain, this theory predicts a λ_+ of 17 m at 70°S and 55 m at 74°S using $K_M = 0.001\ m^2\ s^{-1}$. At ψ_{crit}, $\omega = -f$ (Southern Hemisphere), these equations reduce to

$$\lambda_+ \to \infty \qquad \lambda_- = \sqrt{\frac{-K_M}{2f}}, \tag{7}$$

that is the boundary layer for the positive rotary current becomes infinite. Again, the theory breaks down at ψ_{crit}; nevertheless, good agreement was found between theory and observations in both the Arctic [*Furevik and Foldvik*, 1996] and Weddell Sea [*Foldvik et al.*, 1990]. Thus observations support use of the theory except at ψ_{crit}.

4. Results

4.1. Model Result Considerations

4.1.1. Model outputs. The model output includes cross-slope transects of elevation η and the depth-independent horizontal velocities (U_A and V_A) from the "barotropic mode" and two-dimensional fields of the depth-dependent velocities (U, V, and W), potential temperature θ, and salinity S in the cross-slope (y) and vertical (z) directions from the "baroclinic mode". The vertical velocity W was transformed from sigma coordinates into standard orthogonal coordinates. Hourly fields from the last 2 days for η, U_A, V_A, U, V, and W were analyzed using *Foreman*'s [1977, 1978] tidal analysis routines to obtain the tidal elevation and phases, major axes of the tidal ellipses for both the depth-independent and depth-dependent velocities, and the tidal vertical velocity amplitudes for the M_2 constituent. Additionally, the baroclinic velocities, U_B and V_B, were defined as the difference between the depth-dependent velocity and the depth-independent velocity, $U_B = U - U_A$ and $V_B = V - V_A$ for the along-slope and cross-slope directions, respectively.

4.1.2. Sigma coordinate effects. One drawback of working in sigma coordinates is that false depth-dependent velocities can be generated by the model due to the choice of coordinate system in areas of rapidly changing water depth [*Blumberg and Mellor*, 1987; *Mellor*, 1993]. To determine the magnitude of this false velocity, the model was run without any forcing. Horizontal density gradients induce geostrophic velocities. In order to evaluate the false velocities generated by the topography alone the deep water θ and S profiles (no shelf break front) were used over the entire domain. The maximum false velocities generated were ~0.03 cm s^{-1} in the cross-slope direction and ~0.004 cm s^{-1} in the vertical direction with the largest cross-slope velocities located under the ice shelf and the largest vertical velocities over the continental slope. Over most of the domain these cross-slope velocities were an order of magnitude smaller. With the standard stratification scheme a shelf break front exists in θ and S between the continental shelf and deep basin. In the idealized hydrography used here the changes in θ and S generally compensate for each other with the result that the horizontal potential density gradient across the front is negligible, although a slight gradient exists near the bottom over the upper continental slope. The false velocities resulting from combination of topography and the standard hydrography (shelf break front) were ~0.04 and ~0.005 cm s^{-1} in the cross-slope and vertical directions, respectively. Therefore the false cross-slope velocities associated with the along-slope geostrophic velocities generated by the stratification were roughly equivalent to the false velocities generated by the topography in the sigma coordinate system. These velocity errors are acceptable for our investigation.

4.2. Model Results

Simulations run for transect A showed the amplitudes of the elevation to be constant over nearly the entire transect (Figure 7a), whereas the major axes of the depth-independent velocities vary over the transect increasing with decreasing water column thickness over the continental slope and shelf (Figure 7b). Significant vertical variation occurs in the horizontal depth-dependent velocities for this simulation and is apparent both in the profiles of the cross-slope depth-dependent velocities (Figure 8) at a time near the peak onshore flow and in the major axes of the tidal ellipses for the depth-dependent velocities (Figure 9). Most of the variation occurs in the critical γ region where internal tides are predicted by linear internal wave theory. In this scenario, much of the critical γ region also coincides with the location of the front. The convergence and divergence of the cross-slope velocity profiles near the surface (Figure 8) indicates equatorward propagation of internal tides. Although, the profiles are just a snapshot in time and cannot verify that these motions are internal tides, the major axes for the tidal ellipses confirm that the amplitude of the tidal oscillations is depth-dependent (Figure 9).

4.3. Comparison with Observations

Tidal observations in this region consist of four observations of tidal elevations (stars in Figure 2b) and 19 current meter records measured at nine different moorings (triangles in Figure 2b). Because of the paucity of observations for this region, all nearby tidal observations have been included. The locations of the elevation observations are listed in Table 2, and those of the velocity observations with their depths are listed in Table 3. A fuller discussion of the observations and their uncertainties is given by RPE.

The model results from the simulation with the critical latitude in the domain and with idealized stratification were compared with existing observational data in the region. The elevations predicted by POM disagree slightly with the observations (Table 2) but agree within 0.01 m with the elevation amplitude at the open boundaries. The disagreement between POM and the observations can be attributed to the neglect of the along-slope direction in this application and is discussed more fully in section 4.4.

The major axes predicted by POM for the depth-dependent velocities agree within the uncertainty of the observations for fifteen of the nineteen observations (Table 3). It should be noted that the *Woodgate et al.* [1998] observations were not compared at the distance along the transect corresponding to their latitude but instead to a location along the transect with a similar depth. As a result, these observations, which were made at a location poleward of ψ_{crit}, were compared to model results from a location equatorward of ψ_{crit} where the dynamics differ. The depths for these observations at the corresponding latitude are shown in Table 3, with the depth for the altered location used for the comparison in parentheses. Three of the four velocities which do not agree were within the benthic boundary layer. The mismatch for these points may be due to differences in water depth between the model and observations. At two of the mismatch locations the model and observations have different locations with respect to ψ_{crit}, and the mismatch could be due to differences in the boundary layer thickness. As discussed in section 3.3, the boundary layer thickness is affected by the ψ_{crit}. The fourth mismatch is an overprediction in the midwater column.

From their observations, *Middleton and Foster* [1977] estimated the M_2 tide to be 50% "baroclinic" over the upper continental slope in this region. These observations consisted of a pair of instruments at each of two locations (74^o26'S and 74^o24'S). Both locations had one instrument that was clearly in the benthic boundary layer, either 15 or 25 m from the bottom, and another instrument either 60 or 100 m from the bottom. POM predicts a reduction of velocity of ~67% at the 74^o26' location and 84% at the other (74^o24'), which is closer to the bottom and farther into the benthic boundary layer (Table 3).

4.4. Limitations of the Two-Dimensional Approach

In the Weddell Sea the tides are considered as Kelvin waves propagating along the Antarctic coast [e.g., *MacAyeal*, 1984] and are believed to generally propagate along the slope. Owing to the geometry of the southern Weddell Sea, however, the Kelvin wave splits with a portion of its energy propagating westward along the continental slope and another portion propagating southward across the continental slope following the coast (RPE). A similar situation occurs in the Ross Sea [*MacAyeal*, 1984]. The model domain lies in the region where the coast-following Kelvin wave propagates across the continental slope. However, the two-dimensional transect approach is unable to simulate a Kelvin wave propagating along the coast for this region because a wall does not exist along the eastern boundary of the model domain setting up the elevation gradient and the accompanying pressure gradient necessary for a Kelvin wave. Likewise, the lack of a southern barrier precludes the existence of an along-slope propagating Kelvin wave. The boundary conditions and forcing result in a Poincaré wave at the M_2 frequency propagating along-slope instead. The existence of this Poincaré wave propagating through the domain is supported both by the relative size of the Coriolis force in the terms of the momentum equation and by the ratio of the tidal ellipse axes agreeing with the ratio predicted by linear theory (not shown). Theoretically, Poincaré waves cannot propagate past ψ_{crit}. Therefore, when the critical latitude is in the domain, any north-south portion of the forcing wave is blocked and turned around. As a result, the elevation phase will not increase as it would for a cross-slope propagating wave, and both it and the amplitude remain nearly constant over the domain. Shallow water, flat bottom simulations without ψ_{crit} in the domain and with a large phase difference corresponding to the smaller phase speed for shallow water showed the elevation phase to vary as it would for a propagating wave. An equivalent simulation with ψ_{crit} in the domain showed the elevation phase to be relatively constant but with a maximum at ψ_{crit}, reflecting the blockage of a portion of the Poincaré wave. It should be noted that owing to the long wavelength, not all of the wave energy will be blocked.

5. Summary

A modified version of the Princeton Ocean Model (POM) was used to investigate the generation of internal tides at the M_2 frequency over the outer continental shelf and slope in the southern Weddell Sea. The model was

run as a two-dimensional transect, assuming that bathymetry and tidal forcing were constant in the along-slope direction. Elevations from a barotropic regional model for the northern and southern boundaries were used for boundary conditions.

Linear theory predicts that 10^o equatorward of the M_2 critical latitude ($\psi_{crit}(M_2) \approx 74^o28.5'$), stratification is too weak to support significant generation of internal tides. Near $\psi_{crit}(M_2)$, however, the slope of the internal tidal wave characteristics become flat, and internal tide generation can occur. This latitude is close to the shelf break in the southern Weddell Sea, in a region where much of the interaction occurs between shelf resident water types and the intermediate water types of the deep basin. Thus any mixing associated with the internal tides along the southern shelf would contribute to the water mass mixing that ultimately generates WSDW, which then contributes to the global production of AABW.

The model results agreed well with existing observations. The two-dimensional applications resulted in differences for the elevation amplitudes. However, the amplitudes for the major axes of the tidal ellipses agreed within observational uncertainties for 15 of 19 observation sites, 78%. Most of the sites with disagreements between the model and observational velocities were attributed to differences in location between the locations of the model transect and the observations.

Acknowledgments. I would like to acknowledge my former advisors Laurie Padman and Murray Levine for their advice and useful discussions during my time as a student. I am grateful to Andrew Bennett, John Allen, Ricardo Matano, and Jorge Mesias for their assistance with POM. Peter Holloway's paper on internal tides was of invaluable help. Three anonymous reviewers provided valuable comments on the original manuscript. This work was funded by grant OPP-9896041 from the National Science Foundation and UCSIOPO 10075411 from the National Oceanic and Atmospheric Agency (NOAA). The views expressed herein are those of the author and do not necessarily reflect the views of NOAA or any of its subagencies.

References

Baines, P. G., Internal tides, internal waves, and near-inertial motions, in *Baroclinic Processes on Continental Shelves, Coastal Estuarine Sci. Ser.*, Vol. 3, p. 19-31, AGU, Washington, D. C., 1986.

Blumberg, A. F., and G. L. Mellor, A description of a three-dimensional coastal ocean circulation model, in *Three-Dimensional Coastal Ocean Models, Coastal Estuarine Sci. Ser.*, Vol. 4, edited by N. Heaps, p. 1-17, AGU, Washington, D. C., 1987.

Carmack, E. C., Water characteristics of the Southern Ocean south of the Polar Front, in *A Voyage of Discovery*, edited by M. Angel, pp. 15-41, Pergamon, New York, 1977.

Chen, C., and R. C. Beardsley, Tidal mixing and cross-frontal particle exchange over a finite amplitude asymmetric bank: A model study of Georges Bank, *J. Mar. Res., 56*, 1163-1201, 1998.

Eriksen, C. C., Internal wave reflection and mixing at Fieberling Guyot, *J. Geophys. Res.*, 103, 2977-2994, 1998.

Ffield, A., and A. L. Gordon, Tidal mixing signatures in the Indonesian Seas, *J. Phys. Oceanogr., 26*, 1924-1937, 1996.

Foldvik, A., T. Gammelsrød, N. Slotsvik, and T. Tørresen, Oceanographic conditions on the Weddell Sea shelf during the German Antarctic Expedition 1979/80, *Polar Res., 3*, 209-226, 1982.

Foldvik, A., T. Kvinge, and T. Tørresen, Bottom currents near the continental shelf break in the Weddell Sea, in *Oceanology of the Antarctic Continental Shelf, Antarct,. Res. Ser.*, Vol. 43, edited by S. S. Jacobs, pp. 21-34, AGU, Washington, D. C., 1985.

Foldvik, A., J. H. Middleton, and T. D. Foster, The tides of the southern Weddell Sea, *Deep Sea Res., 37*, 1345-1362, 1990.

Foreman, M. G. G., Manual for tidal height analysis and prediction, *Pac. Mar. Sci. Rep. 77-10*, 58 pp., Inst. of Ocean Sci., Patricia Bay, Sidney, British Columbia, Canada, 1977.

Foreman, M. G. G., Manual for tidal current analysis and prediction, *Pac. Mar. Sci. Rep. 78-6*, 70 pp., Inst. of Ocean Sci., Patricia Bay, Sidney, British Columbia, Canada, 1978.

Foster, T. D., Large, steplike temperature and salinity structures observed in the central Weddell Sea, *Antarct. J., 29*, 99-100, 1994.

Foster, T. D., and E. C. Carmack, Frontal zone mixing and Antarctic Bottom Water formation in the southern Weddell Sea, *Deep Sea Res., 23*, 301-317, 1976.

Foster, T. D., A. Foldvik, and J. H. Middleton, Mixing and bottom water formation in the shelf break region of the southern Weddell Sea, *Deep Sea Res., 34*, 1771-1794, 1987.

Furevik, T., and A. Foldvik, Stability at M_2 critical latitude in the Barents Sea, *J. Geophys. Res., 101*, 8823-8837, 1996.

Gammelsrød, T., A. Foldvik, O. A. Nøst, Ø. Skagseth, L. G. Anderson, E. Fogelqvist, K. Olsson, T. Tanhua, E. P. Jones, and S. Østerhus, Distribution of water masses on the continental shelf in the southern Weddell Sea, in *The Polar Oceans and Their Role in Shaping the Global Environment, Geophys. Monogr. Ser*. Vol. 84, p. 159-176, AGU, Washington, D.C., 1994.

Gill, A. E., *Atmosphere-Ocean Dynamics*, 662 pp., Academic, San Diego, Calif., 1982.

Gordon, A. L., Western Weddell Sea thermohaline stratification, in *Ocean, Ice and Atmosphere: Interactions at the Antarctic Continental Margin, Antarct. Res. Ser.*, Vol. 75, edited by S. S. Jacobs and R. Weiss, pp. 210-240, AGU, Washington, D. C., 1998.

Haltiner G. J., and R. T. Williams, *Numerical Prediction and Dynamic Meteorology*, 477 pp., John Wiley, New York, 1980.

Hatayama, T., T. Awaji, and K. Akitomo, Tidal currents in the Indonesian Seas and their effect on transport and mixing, *J. Geophys. Res., 101*, 12,353-12,373, 1996.

Holloway, P. E., A numerical model of internal tides with application to the Australian northwest shelf, *J. Phys. Oceanogr., 26*, 21-37, 1996.

Huber, B.A., P. A. Mele, W. E. Haines, A. L. Gordon, and V. I. Lutkin, Ice Station Weddell, 1, CTD/hydrographic data, *Tech. Rep. LDEO 94-2*, Lamont-Doherty Earth Obs., Palisades, N. Y., 1994.

Huthnance, J. M., Internal tides and waves near the continental shelf edge, *Geophys. Astrophys. Fluid Dyn., 48*, 81-105, 1989.

Lamb, H., *Hydrodynamics*, 738 pp., Dover, Mineola, N. Y., 1945.

Le Blond, P. H., and L. A. Mysak, *Waves in the Ocean*, 602 pp., Elsevier Sci., New York, 1978.

Le Tareau, J. Y., and R. Maze, On barotropic and baroclinic tides over an arbitrary sloping topography, *Ann. Geophys., 14*, 961-975, 1996.

Levine, M. D., L. Padman, R. D. Muench, and J. H. Morison, Internal waves and tides in the western Weddell Sea: Observations from Ice Station Weddell, *J. Geophys. Res, 102*, 1073-1089, 1997.

Lewis, J. K., Y. L. Hsu, and A. F. Blumberg, Boundary forcing and a dual-mode calculation scheme for coastal tidal models using step-wise bathymetry, in *Estuarine and Coastal Modeling III, Proceedings of the 3rd International Conf., Oakbrook, IL, Sept. 1993*, edited by M. L. Spaulding et al , pp. 422-431, Am. Soc. of Civ. Eng., New York, 1994.

MacAyeal, D. G., Numerical simulation of the Ross Sea tide, *J. Geophys. Res, 89*, 607-615, 1984.

Makinson, K., and K. W. Nicholls, Modeling tidal currents beneath Filchner-Ronne Ice Shelf and on the adjacent continental shelf: Their effect on mixing and transport, *J. Geophys. Res, 104*, 13,449-13,465, 1999.

Martinsen, E. A., and H. Engedahl, Implementation and testing of a lateral boundary scheme as an open boundary condition in a barotropic ocean model, *Coasal. Eng., 11*, 603-627, 1987.

Mellor, G. L., User's guide for a three-dimensional, primitive equation, numerical ocean model., 35 pp., Atmos. and Ocean Sci. Program, Princeton Univ., Princeton, N. J., 1993.

Middleton, J. H., and T. Denniss, The propagation of tides near the critical latitude, *Geophys. Astrophys. Fluid Dyn., 68*, 1-13, 1993.

Middleton, J. H., and T. D. Foster, Tidal currents in the central Weddell Sea, *Deep Sea Res., 24*, 1195-1202, 1977.

Middleton, J. H., T. D. Foster, and A. Foldvik, Low-frequency currents and continental shelf waves in the southern Weddell Sea, *J. Phys. Oceanogr., 12*, 618-634, 1982.

Munk, W., and C. Wunsch, The moon and mixing: Abyssal recipies II, *Deep Sea Res. Part I, 45*, 1977-2010, 1998.

National Geophysical Data Center, GEODAS CD-ROM Worldwide marine geophysical data, *Data Announce. 92-MGG-02*, Natl. Oceanic and Atmos. Admin., Boulder, Colo., 1992.

Oey, L.-Y., G. L. Mellor, and R. I. Hires, A three-dimensional simulation of the Hudson-Raritan Estuary, part I, Description of the model and model simulations, *J. Phys. Oceanogr., 15*, 1676-1692, 1985a.

Oey, L.-Y., G. L. Mellor, and R. I. Hires, A three-dimensional simulation of the Hudson-Raritan Estuary, part III, Salt flux analyses, *J. Phys. Oceanogr., 15*, 1711-1720, 1985b.

Padman, L., A. J. Plueddemann, R. D. Muench, and R. Pinkel, Diurnal tides near the Yermak Plateau, *J. Geophys. Res, 97*, 12,639-12,652, 1992.

Padman, L., R. Robertson, and K. Nicholls, Modeling tides in the southern Weddell Sea: Updated model with new bathymetry from ROPEX, *Rep. 12*, pp. 65-73, Fichner-Ronne Ice Shelf Programme, Bremerhaven, Germany, 1999.

Palma, E. D., and R. P. Matano, On the implementation of passive open boundary conditions for a general circulation model: The barotropic mode, *J. Geophys. Res. 103*, 1319-1342, 1998.

Petruncio, E. T., Observations and modeling of the internal tide in a submarine canyon, Ph.D. thesis, 181 pp., Naval Postgrad. Sch. at Monterey, Calif., Sept. 1996.

Polyakov, I.V., Maintenance of the Arctic Ocean large-scale baroclinic structure by the M_2 tide, *Polar Res., 13*, 219-232, 1995.

Polzin, K. L., J. M. Toole, J. R. Ledwell, and R. W. Schmitt, Spatial variability of turbulent mixing in the abyssal ocean, *Science, 276*, 93-96, 1997.

Prinsenberg, S. J., and E. B. Bennett, Vertical variations of tidal currents in shallow land fast ice-covered regions, *J. Phys. Oceanogr., 19*, 1268-1278, 1989.

Robertson, R., Mixing and heat flux mechanisms in the upper ocean in the Weddell Sea, Ph.D. thesis, 173 pp., Oreg. State Univ., Corvallis, Feb. 1999.

Robertson, R., Internal tides and baroclinicity in the southern Weddell Sea, 2, Effects of the critical latitude and stratification, *J. Geophys. Res.*, this issue.

Robertson, R., L. Padman, M. D. Levine, R. D. Muench, and M. G. McPhee, Internal waves in the eastern Weddell Sea during AnzFlux, paper presented at IAPSO XXI General Assembly, Honolulu, Hawaii, 1995.

Robertson, R., L. Padman, and G. D. Egbert, Tides in the Weddell Sea, in *Ocean, Ice and Atmosphere: Interactions at the Antarctic Continental Margin, Antarct. Res. Ser.,Vol*, 75, edited by S. S. Jacobs and R. Weiss, pp. 341-369, AGU, Washington, D. C., 1998.

Robertson, R., L. Padman, and M. D. Levine, A correction to the baroclinic pressure gradient term in the Princeton Ocean Model, *J. Atmos. Ocean. Tech., 18*, 1068-1075, 2001

Sherwin, T. J., Evidence of a deep internal tide in the Faeroe-Shetland Channel, in *Tidal Hydrodynamics*, edited by B. B. Parker, pp. 469-488, John Wiley, New York, 1991.

Sjöberg, B., and A. Stigebrandt, Computations of the geographical distribution of the energy flux to mixing processes via internal tides and the associated vertical circulation in the ocean, *Deep Sea Res., 39*, 269-291, 1992.

Sverdrup, H. U., Dynamics of tides on the North Siberian Shelf: Results from the Maud expedition, *Geophys. Norv. 4*, Oslo, 75 pp., 1927,

Thiel, E., A. P. Crary, R. A. Haubrich, and J. C. Behrendt, Gravimetric determination of ocean tide, Weddell and Ross Seas, Antarctica, *J. Geophys. Res., 65*, 629-636, 1960.

Vaughan, D. G., J. Sievers, C. S. M. Doake, G. Grikurov, H. Hinze, V. S. Pozdeev, H. Sandhäger, H. W. Schenke, A. Solheim, and F. Thyssen, Map of the subglacial and seabed topography; Filchner-Ronne-Schelfeis/Weddell Sea, Antarktis, scale 1:2,000,000, Inst. für Angewandte Geodäsie, Frankfurt am Main, Germany, 1994.

Weppernig, R. P., Schlosser, S. Khatiwala, and R. G. Fairbanks, Isotope date from Ice Station Weddell: Implications for deep water formation in the Weddell Sea, *J. Geophys. Res., 101*, 25,723-25,739, 1996.

Woodgate, R. A., M. Schröder, and S. Østerhus, Moorings from the Filchner Trough and the Ronne Ice Shelf Front: Preliminary results, *Rep. 12*, pp. 85-90, Filchner-Ronne Ice Shelf Programme, Alfred-Wegener Inst., Bremerhaven, Germany, 1998.

Xing, J., and A. M. Davis, Processes influencing the internal tide, its higher harmonics, and tidally induced mixing on the Malin-Hebrides Shelf, *Prog. in Oceanogr., 38*, 155-204, 1996.

R. Robertson, Lamont-Doherty Earth Observatory,
Columbia University, Route 9W, Palisades, NY 10964, USA
(rroberts@ldeo.columbia.edu)

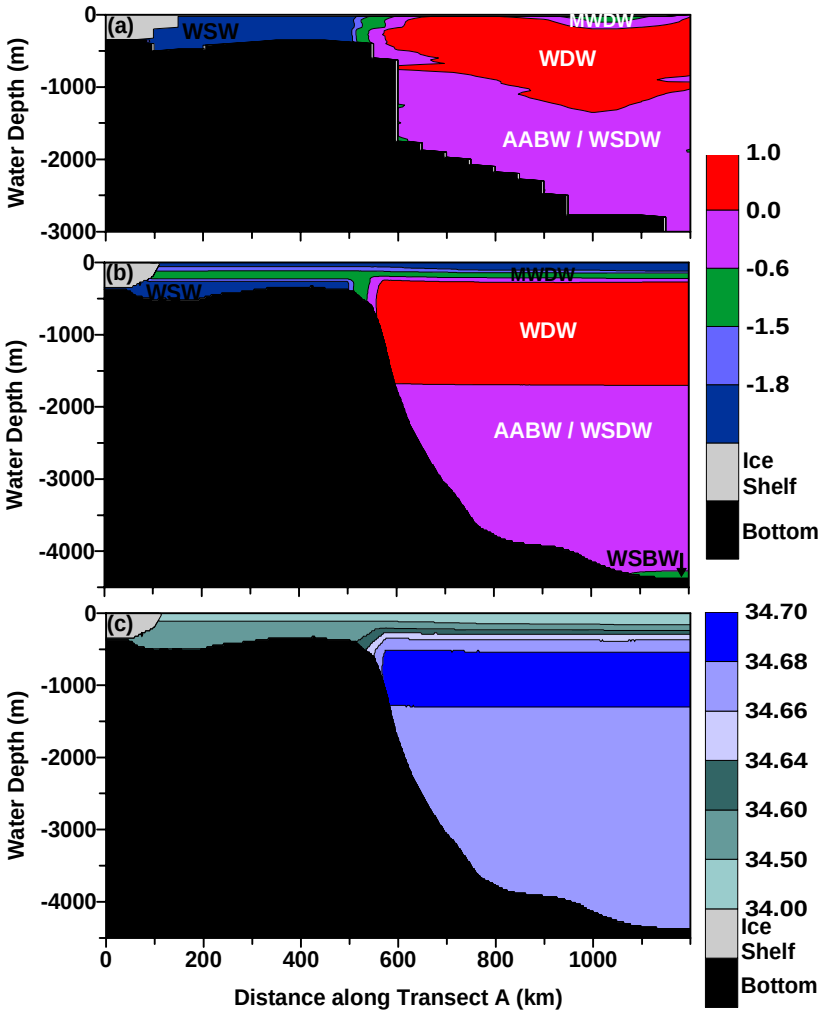

Figure 1. (a) The observed potential temperature θ along the transect estimated using a Gaussian weighted average and the initial (b) potential temperature θ and (c) salinity S conditions used for the simulations. The ice shelf is indicated by shading and the bottom is indicated by black. Several water masses have been identified in Figures 1a and 1b. These include Western Shelf Water (WSW), Modified Warm Deep Water (MWDW), Warm Deep Water (WDW), Weddell Sea Deep Water (WSDW) or Antarctic Bottom Water (AABW), and Weddell Sea Bottom Water (WSBW). Ice Shelf Water (ISW) and Winter Water (WW) are not indicated.

Part 1 Figure 2

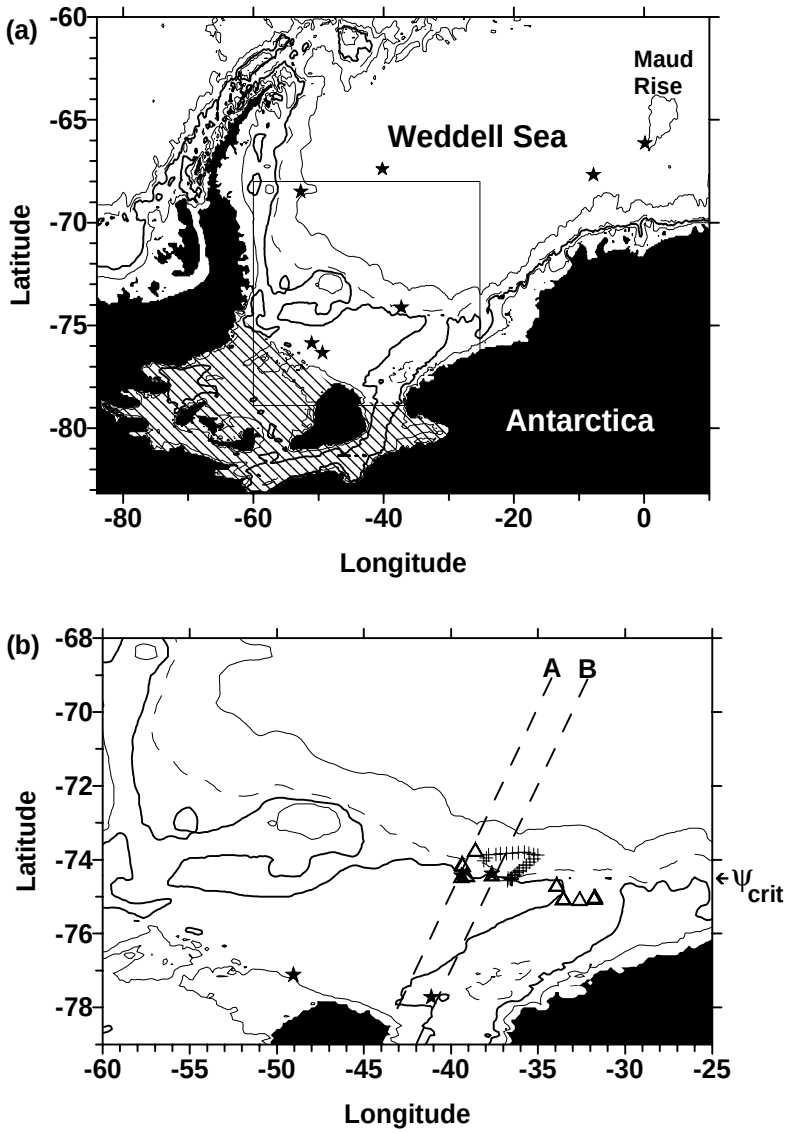

Figure 2. (a) The water column thickness for the Weddell Sea, contoured at 200, 500 (thick line), 1000 (dashed line), and 3000 m. The Filchner-Ronne Ice Shelf area is indicated by hatching. Stars indicate the location of observations of internal tides. (b) The water column thickness for the boxed region in Figure 2a with identical contouring intervals. The location of the transects used for the model domain are shown as dashed lines. The location of observations of tidal elevations are indicated by stars, those of tidal currents are indicated by triangles, and those of the Ropex profiles are indicated by crosses. The location of the M_2 critical latitude is indicated by ψ_{crit} on the right axis.

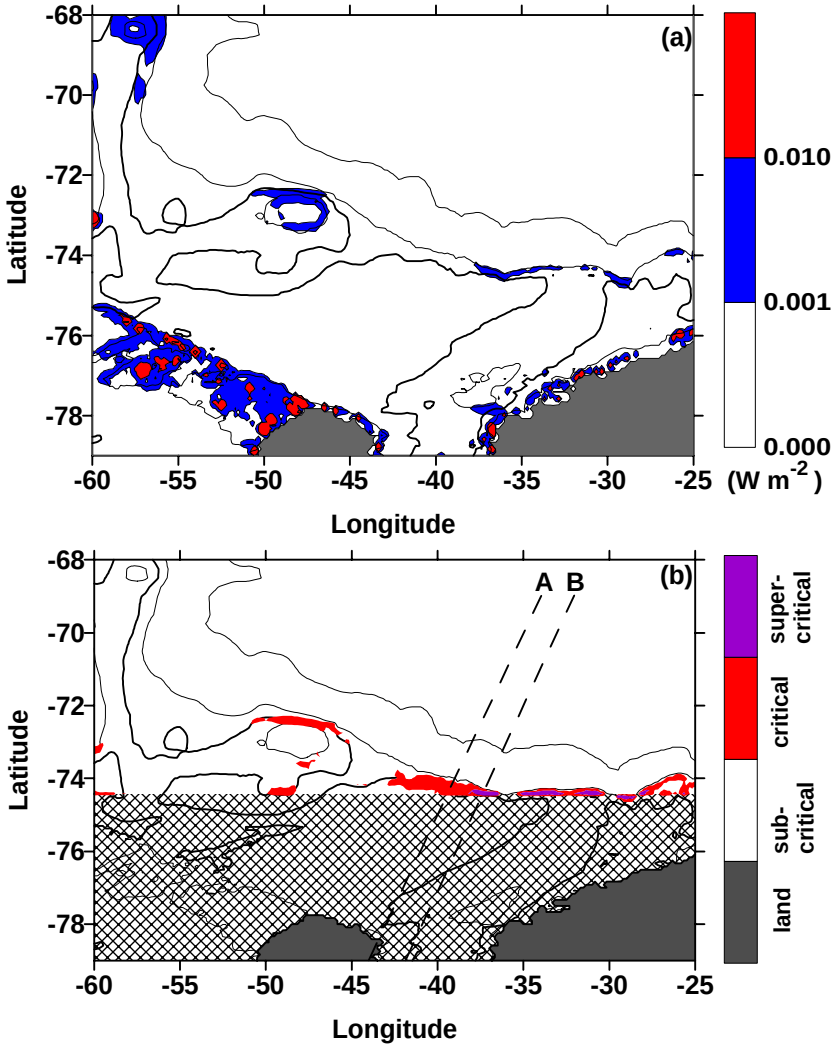

Figure 3. (a) The energy loss from the barotropic tide to the baroclinic tide as determined by *Robertson et al.* [1998] following the method of *Sjöberg and Stigebrandt* [1992]. (b) The internal wave generation criteria parameter $\gamma(M_2)$ for the Weddell Sea. The locations of the transects are shown as dashed lines. The subcritical, critical, and supercritical regimes of $\gamma(M_2)$ are indicated. Water column thickness is contoured at 200, 500 (thick line), 1000, and 3000 m in both Figures 3a and 3b. In Figure 3b, the area poleward of the critical latitude where the linear theory is no longer applicable is indicated by hatching. Here $\gamma(M_2)$ is defined as zero for flat slopes.

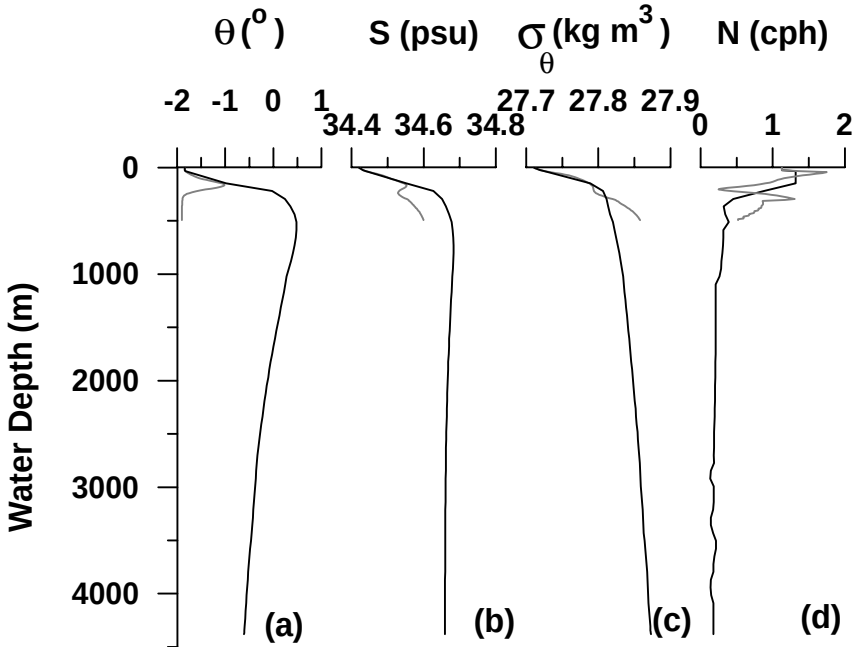

Figure 4. The (a) potential temperature θ, (b) salinity S, (c) potential density σ_θ, and (d) Brunt-Väisälä frequency N profiles for the stratification over the deep basin (solid line) and the continental shelf (shaded line).

Part 1 Figure 5a

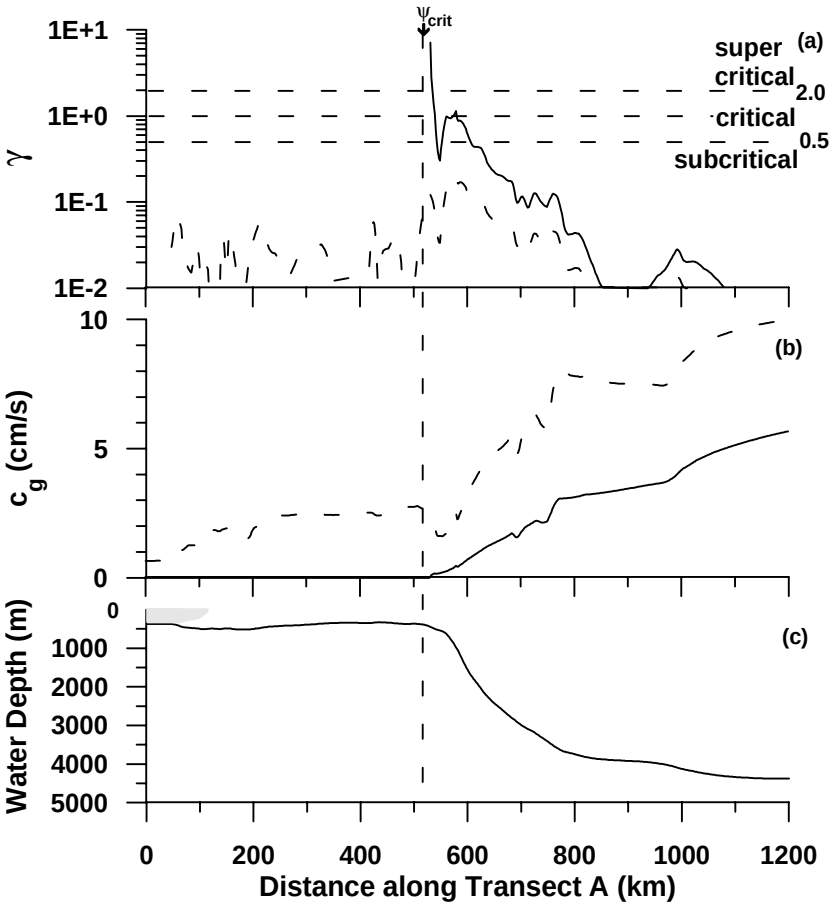

Figure 5. (a) The internal wave generation criterion parameter $\gamma(M_2)$, (b) the internal wave horizontal group speed c_g, and (c) the water depth D and ice shelf thickness for transect A with the hypothetical winter stratification. In Figures 5a and 5b the values when transect A is in the actual location are indicated by black lines and by dashed lines when the transect A is shifted 10^o north so the critical latitude is not present in the domain. The critical, subcritical, and supercritical ranges are denoted in Figure 5a. The location of the M_2 critical latitude is denoted with a dashed line and ψ_{crit}. (d-f) The corresponding fields for a transect B with the same stratification as in Figures 5a-5c.

Part 1 Figure 5a

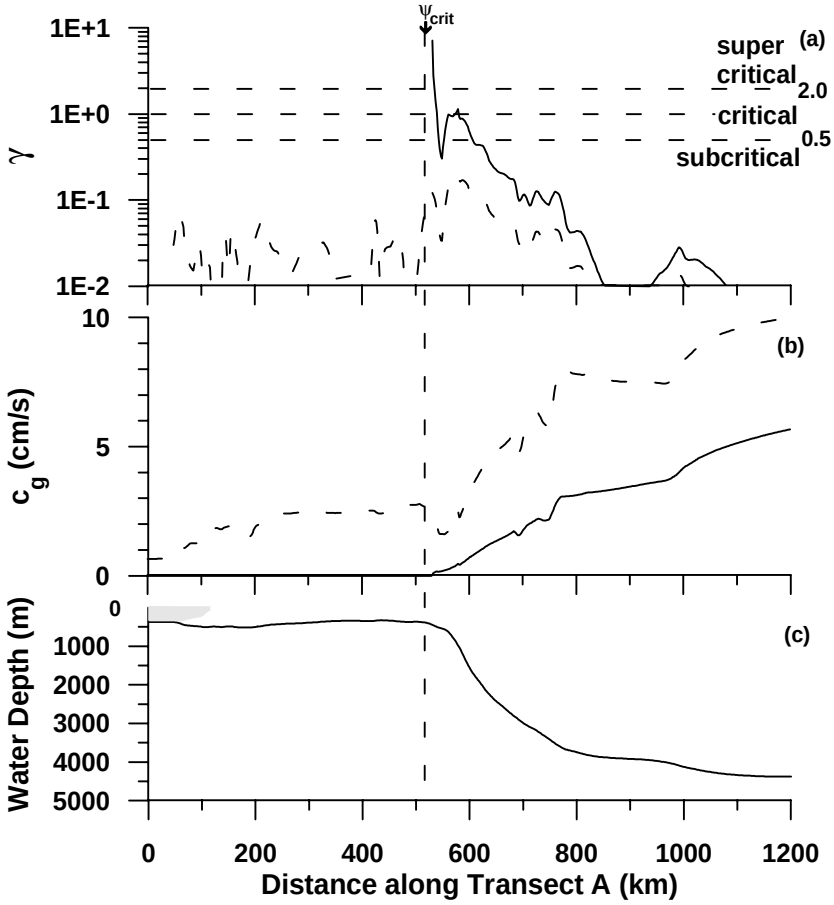

Figure 5. (continued)

Part 1 Figure 6

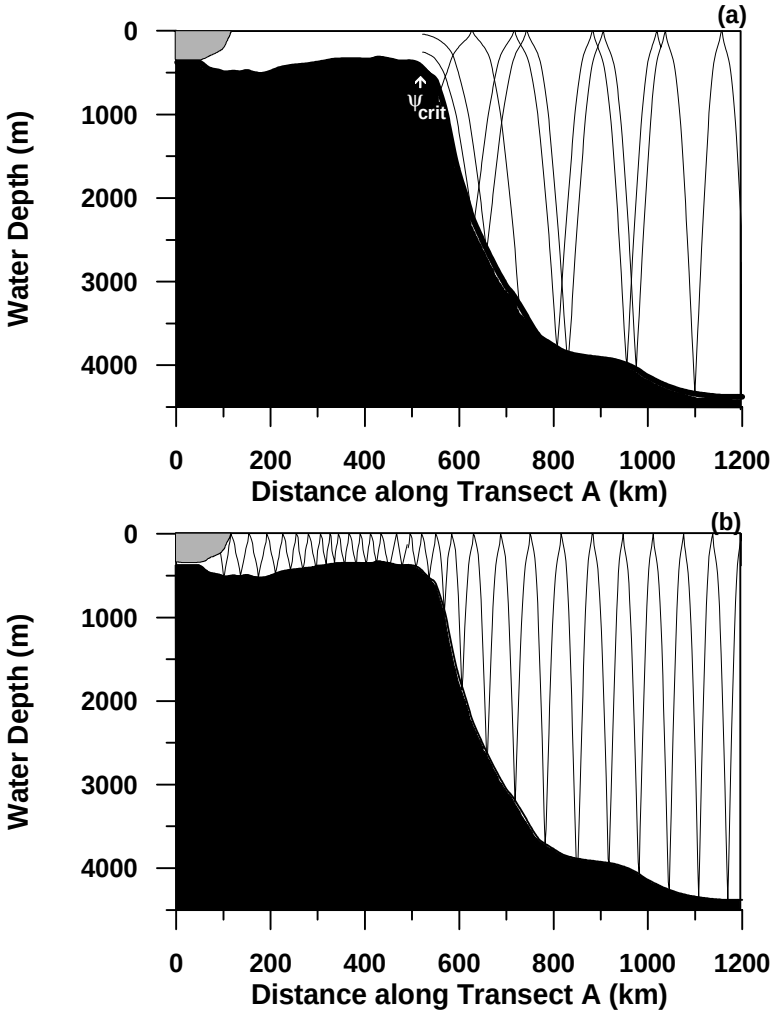

Figure 6. Characteristic internal waves ray paths for the M_2 tide for transect A (a) with the critical latitude present in the domain and (b) without the critical latitude in the domain. The location of the critical latitude is indicated by ψ_{crit} in Figure 6a.

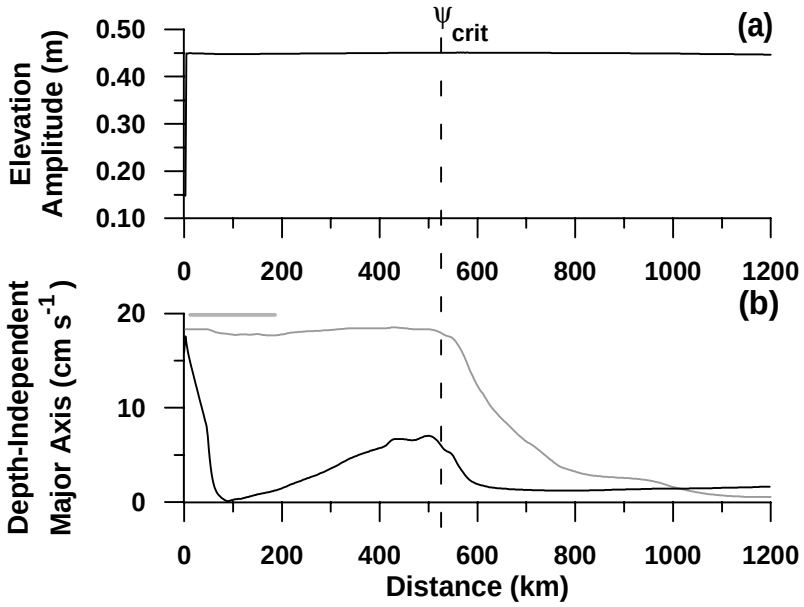

Figure 7. (a) The elevation amplitude from simulations with a stratified ocean with the critical latitude crossing through the domain. (b) The major axis of the depth-independent velocities from a simulation with the M_2 critical latitude crossing through the domain. The topography is indicated in Figure 7b by thick shaded lines. The location of the critical latitude is denoted with ψ_{crit} in Figure 7a.

Part 1 Figure 8

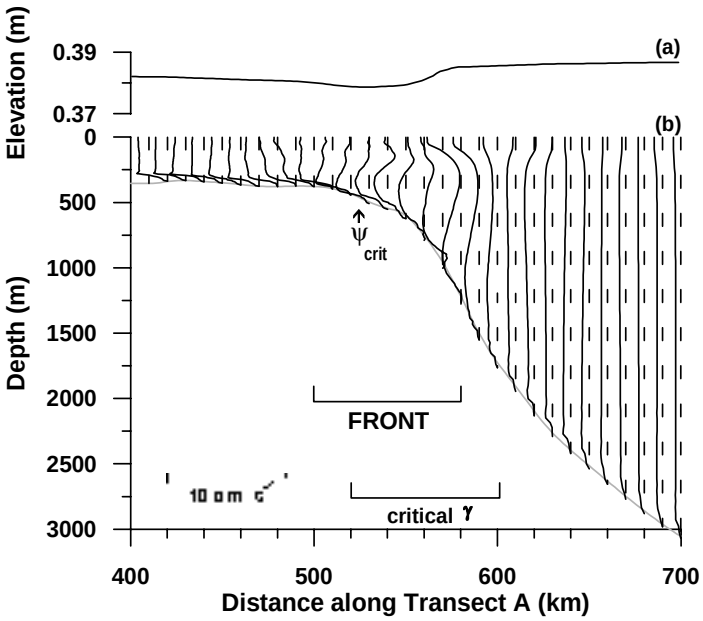

Figure 8. (a) Elevation along the transect from a simulation with stratification for transect A (at t = 45.625 days). (b) Cross-slope velocity profiles over the continental slope from the same simulation. The locations of ψ_{crit} and the front and critical γ ranges are indicated in Figure 8b. Dashed lines representing zero velocity are included for each profile.

Part 1 Figure 9

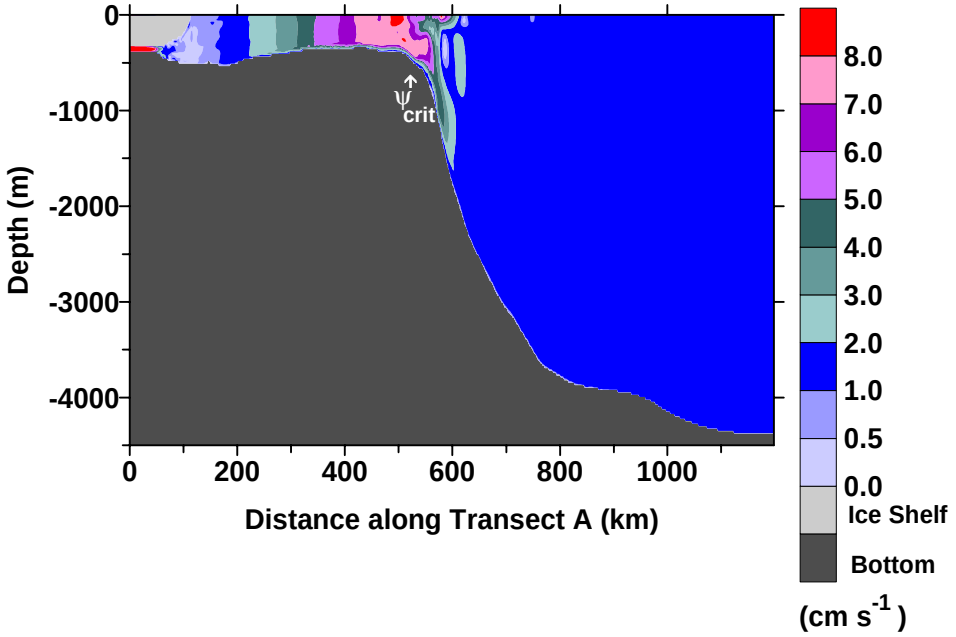

Figure 9. The major axes of the tidal ellipses from a simulation with stratification for transect A. The location of the critical latitude is denoted in by $\psi_{cr.}$